Analytical and numerical crashworthiness uncertainty quantification of metallic thin-walled energy absorbers

J. Paz[a,*], J. Díaz[a], L. Romera[a]

[a]*Universidade da Coruña – Structural Mechanics Group, School of Civil Engineering. 15071, Spain*

Abstract

Thin-walled tubular components are featured in transport structures for increased occupant protection in the event of a crash. However, when the limits of their design are sought through deterministic procedures, components often become unreliable due to uncertainties which may cause them to underperform or even fail. Seeking a deeper understanding of the effect of incertitudes on the thin-walled tubes' performance, this research focuses on the crashworthiness quantification of diverse sources of uncertainties in the progressive collapse of these components under axial loads. For a broader insight on the tubes' behavior, diversity is considered and scrutinized on all the main fields involved in the research; studying two cross-sections, three sources of uncertainties, and the two epitomical crashworthiness metrics, namely the average and peak crushing loads. The process is undertaken via three different methods, combining analytical formulas, numerical simulations, and surrogate modeling. Results show that the best approximation is offered by the multivariate adaptive regression splines metamodel, yielding similar mean values as with the statistical propagation of the analytical formulas, while the standard deviation is overestimated by 1% to 3%. The numerical noise quantified for the simulations results shows oscillation frequencies below 40% and a breadth of three-sigma under 9% for both metrics. The uncertainty quantification of both tubes offers a similar response when studying geometric uncertainties, with the plate thickness having a more relevant effect on the results than diameter or edge length. However, material uncertainties affect the absorbers in an opposite manner, as variations in the elastic modulus contribute the most to the square section metrics, while the circular tube is more affected by variations in the equivalent flow stress. Incertitudes in the operational conditions lead to reduced peak load values when the impact angle varies from a perfect axial collision, consequently delivering reduced mean values and high standard deviations.

Keywords: Crashworthiness, uncertainty quantification, crushable energy absorbers, surrogate models

1. Introduction

Thin-walled crushable tubular structures are among the most common energy absorption devices used for passenger protection in transport vehicles. They can be featured as structural elements in aircraft and helicopter sub-floor structures [1–3], front deformation areas for cars [4, 5] or trains [6], and even as roll-over protection structures on construction machinery [7]. In the event of a crash, these energy absorbers are designed to collapse progressively, dissipating high amounts of kinetic energy through plastic deformation to protect the passengers against abrupt deceleration [8]. As Alghamdi [9] identified, their shape and thickness-to-weight ratios are similar independently of the scale difference between means of transportation. Their energy dissipation profile is influenced by many factors, as the magnitude and application of the load, the strain-rate sensitivity of the materials, or the deformation mode occurring [10].

The collapse of thin-walled tubes can unfold under several modes depending on their cross-section shape, load direction, and the ratios between cross-sectional inertia, length, and wall thickness [11]. Since the first studies on collapsible tubes from

J. M. Alexander [12], significant efforts have been made to further understand their behavior by using different cross-sections [13, 14], materials [15], collapse modes [16, 17], or reinforcing cores [18]. Axial crushing is the most common energy dissipating method, primarily due to its high capabilities as an energy dissipation device [19]. When compared to other deformation modes, axial energy dissipation values can be up to ten times higher for the same tube, as proved by Reid [20]. In the case of circular metallic tubes, their progressive axial crushing can develop under three different configurations [17]: an axisymmetric concertina mode, the non-axisymmetric diamond collapse with slightly lower specific energy absorption than the former [21], and a mixed collapse mode. Analogously, the progressive collapse of square cross-sections can unfold under symmetric, asymmetric, or mixed modes; with the symmetric offering the highest specific energy absorption capabilities [22].

The current widespread method for the prediction of the crush behavior of thin-walled tubes dwells in the use of computational models and finite element analyses (FEAs), considered first-principles or fully predictive methods. The use of FEAs allows to accurately mimic the experimental process [23], reduces expenses, and enables the assessment of a wider range of models and impact conditions than experiments. However, and despite the many advancements implemented in FEA to

---

*Corresponding author. Tel: +34 881 016 107.

Email address: `javier.paz.mendez@udc.es` (J. Paz)

improve simulation's computational time, robustness, and accuracy, certain shortcomings as noise and repeatability still affect the fidelity of non-linear dynamic analyses [24]. Moreover, the explicit time step scheme, memory parallelization, and contact formulation used in such non-linear simulations lead to results not often repeatable [25], which may even trigger the extreme example of bifurcation where unique structural reaction patterns appear [26, 27].

When these structures are designed, modeled, and optimized via deterministic processes, no room is left for the consideration of the uncertainties involved in real-life engineering problems. One tool for the preliminary design of more robust structures is that of parameter screening and selection, where the effect of varying the design parameters along their feasible domain is assessed to determine which have the largest influence on the monitored metrics [28, 29].

Moreover, uncertainty quantification (UQ) methods propagate incertitudes to the desired objective metrics, obtaining responses in the form of a probabilistic function with its own statistical moments. The uncertainty variables typically used in crashworthiness applications are classified into three sources depending on their nature: operational, manufacturing, and modeling [30]. Operational uncertainties include those as impact conditions, commonly considered in UQ analyses since small variations of the impact angle and velocity can severely influence the component's structural response [31, 32]. Geometry uncertainties fall within the manufacturing type, and are also typically studied [33–35] with authors as Eichmueller and Meywerk [36] proving that slight thickness variations in axially-loaded square tubes can cause relevant dispersion of the component's behavior both at low and high testing speeds. Uncertainties in the value of material properties as the elastic and tangential moduli, Poisson's ratio, density, or the yield stress can also be considered to account for the discrepancies induced by the manufacturing process between the nominal design and the resulting real product [37, 38].

Modeling uncertainties relate to mathematical and numerical modeling techniques for extracting the component's crashworthiness performance, as numerical error in FEAs or errors within a surrogate model. Surrogate models (or metamodels) are an efficient tool for the characterization of manufacturing and operational phenomena, substituting the real responses by approximate functions obtained from a series of sampling evaluations, in which the design space is surveyed using sampling methods. This significantly reduces computational costs during UQ and, specially, for the more computationally-demanding reliability-based design optimization (RBDO) procedures [39]. However, the main issue with the use a surrogate model dwells in its accuracy, as substituting the real functions by a numerical model may also introduce metamodeling uncertainty to the results [40, 41]. Moreover, if the metrics are obtained from FEAs, it can also contribute as a source of error and should also be considered in the crashworthiness design process as performed by authors as Zhang et al. [42] or Zhu et al. [24].

However, and to the best of the authors' knowledge, no research is currently available in which all three types of uncertainties are considered and addressed in-depth as to characterize and rank how the crashworthiness of thin-walled structures is affected by these uncertainties. Motivated by this, the following research first investigates the behavior of energy absorption components' due to uncertainties in structural dimensions, material properties, initial impact conditions, and the numerical simulation. In a first approach, the analytical uncertainty propagation of the most representative analytical formulas for average and peak crushing loads is addressed for the two selected tube geometries used, namely square and circular. Realistic values are used for the design variables' statistical parameters, quantifying the robustness of the components under different uncertainty conditions. Considering that the variables are the sum of many random processes, and according to the Central Limit Theorem, all design variables are assumed to follow a Gaussian distribution. These variables are also screened and ranked in a correlation matrix according to their influence on the final crashworthiness response.

Later, the UQ process is repeated numerically for these analytical formulas by coupling them with the metamodeling code. A latin hypercube sampling is performed over the design space as to fit and compare different surrogate models, seeking the most compliant metamodel to achieve trustworthy designs and results. The fitness of the metamodels is assessed according to statistical metrics, determining those most compliant with the analytical results previously obtained. The final step in the investigation substitutes the analytical formulas by FEAs for the sampling and construction of the surrogate model. In this phase, the numerical simulation noise is quantified following a similar approach as Gilkeson et al. [43] by decomposing the oscillation noise into frequency and amplitude. The statistical results from the studied metrics are compared to the results previously obtained as to determine the inaccuracies yielded by the FEAs.

This research combines the uncertainty quantification approaches and techniques from previous works, later applying it to assess the crashworthiness response of energy absorption tubes under impact scenarios. With the following investigation we attempt to advance a step forward in the reliable and robust design of energy absorbing components for crashworthiness applications, offering in-depth analyses of the effect of different types of uncertainties on the crashworthiness performance of thin-walled energy absorbers.

2. Analytical models

The first phase of this research focuses on the analytical characterization and crashworthiness uncertainty quantification of circular and square thin-walled tubes under axial loading. A baseline model is selected for each geometry, both being modeled with the AA2024-T3 aluminum alloy detailed in table 1, considering its widespread use in such crashworthiness applications. Since the analytical formulas used do not allow the inclusion of strain-rate effects or even a plasticity curve different than a bilinear model, the aluminum is idealized for the sake of comparison with the numerical models used later in the research. Thus, the material is defined by its Young's modulus E, the energy equivalent flow stress σ_0 (an average value of stress along the stress-strain curve from the initial strain to its final

value), the transverse elastic modulus E_t, the yield stress σ_y, the final strain ε_u, the Poisson ratio ν, and the density ρ. All the aforementioned parameters are required throughout the research, although some may not be directly considered depending on the nature of the analysis. Table 1 also contains the mean and standard deviation values for the two material random variables selected, the Young's modulus and the energy equivalent flow stress, with three different coefficients of variation (COV) considered for each random variable to further understand the effect of these uncertainties on the performance of thin-walled tubes.

Parameter	Mean	Standard deviation		
		COV = 2 %	COV = 5 %	COV = 10 %
E (GPa)	73.10	1.462	3.655	7.310
σ_0 (MPa)	280.0	5.60	14.00	28.00
E_t (MPa)	60.0	-	-	-
σ_y (MPa)	250	-	-	-
ε_u	0.2	-	-	-
ν	0.33	-	-	-
ρ (kg/m^3)	2700.0	-	-	-

Table 1: Properties of AA2024-T3 aluminum alloy and statistical parameters. Three different coefficients of variation are considered for the Gaussian random variables E and σ_0; while E_t, σ_y, ν, and ρ are deterministic.

2.1. Metrics and notation

The metrics for the study of the crashworthiness performance of the tubes, the average and peak crushing loads, have been selected given their simplicity and widespread use. Other more complex functions are commonly used in crashworthiness studies, although there may not exist analytical formulas for those or they are derived from the ones here considered. The notation used has been selected to particularize each tube shape, source of the result, and the metric in question. It takes the form $P^x_{y\text{-}z}$ where x can be 'emp' for the empirical analytical formula, 'theo' for the theoretical analytical formula, or 'FEA' if stemming from numerical simulations. The tube shape is defined by y, where 'c' and 's' stand for circular and square cross-sections respectively. Finally, z indicates the metric studied, with 'mean' relating to the average crushing force and 'max' to the peak force. As for statistic-related notation, $E[\ ]$ is used to denote the expected value, $V[\ ]$ refers to the variance, and $\sigma[\ ]$ is the standard deviation.

2.2. Circular tube

The circular tube geometry is defined by a diameter of $D = 80$ mm and a plate thickness of $t_c = 2$ mm, resulting in a D/t_c ratio of 40 which ensures the tube's collapse under the concertina mode for higher energy absorption [17]. These random design variables are assumed to behave according to a normal distribution, with their statistical moments defined in table 2.

Three different coefficients of variation are used for each variable.

Design variable	Mean	Standard deviation		
		COV = 2 %	COV = 5 %	COV = 10 %
D (mm)	80.00	1.60	4.00	8.00
t_c (mm)	2.00	0.04	0.10	0.20

Table 2: Statistical moments for the geometrical random design variables of the circular tube.

Two analytical formulas are chosen for the prediction of their peak crushing force $P_{c\text{-max}}$, and one for the average crushing force, $P_{c\text{-mean}}$. Crashworthiness-oriented research tends to use the components' energy absorption as a metric rather than $P_{c\text{-mean}}$, although the former is the average force times the crushing distance, thus representing a homologous consideration of the crashworthiness performance by the specimen. The empirical formula from Guillow et al. [17] estimates $P_{c\text{-mean}}$ as

$$P^{\text{emp}}_{c\text{-mean}} = 72.3(D/t_c)^{0.32}M_0, \tag{1}$$

with M_0 being the fully plastic bending moment based on the flow stress, defined as $M_0 = \sigma_0\, t_c^2/4$. Abramowicz and Jones [44], focusing on the theoretical energy dissipation from plastic hinge formation, predict the average force by

$$P^{\text{theo}}_{c\text{-mean}} = \frac{25.23\,\sqrt{D/t_c} + 15.09}{0.86 - 0.568\,\sqrt{t_c/D}}\,M_0. \tag{2}$$

On the other hand, $P_{c\text{-max}}$ is estimated with the formulas from Plantema [45] as

$$P^{\text{theo}}_{c\text{-max}} = \begin{cases} \sigma_0\, A^c_S & \text{for } \alpha \geq 8 \\ (0.75 + 0.031\alpha)\,\sigma_0\, A^c_S & \text{for } 2.5 \leq \alpha < 8 \\ 0.3\,\alpha\,\sigma_0\, A^c_S & \text{for } \alpha < 2.5, \end{cases} \tag{3}$$

where A^c_S is the cross-sectional area for the circular tube, calculated as $A^c_S = \pi D\, t_c$. The parameter α is calculated as:

$$\alpha = \frac{E\, t_c}{\sigma_0\, D} \tag{4}$$

For the studied circular tube, $\alpha \approx 6$.

To quantify the effect of uncertainties in the design variables, the analytical error propagation of these formulas is performed using the approximations from Hendeby and Gustafsson [46]. The integration process to reach the formulas for the error propagation is detailed in Appendix A.

Finally, two dimensionless ratios introduced by Pugsley [47] are studied to assess the efficiency of the thin-walled structures, the structural effectiveness η and the solidity ratio ϕ. The solidity ratio, also called relative density, is the ratio between cross-

sectional area A_S and wall cross-sectional area A_C (defined as the area enclosed by the tube's cross-section), calculated for the circular tube as:

$$\phi^c = \frac{A_S^c}{A_C^c} = \frac{\pi D\, t_c}{\pi (D/2)^2} = \frac{4t_c}{D}, \tag{5}$$

while the structural effectiveness for the circular tube can be obtained from the theoretical formula as

$$\eta_{\text{theo}}^c = \frac{P_{\text{c-mean}}}{\pi D\, t_c\, \sigma_0} = \sqrt{\frac{\pi \phi}{2\sqrt{3}}} \tag{6}$$

and from the empirical formula from Thornton et al. [48]

$$\eta_{\text{emp}}^c = 2(\phi^c)^{0.7}. \tag{7}$$

Particularized for the selected geometry, these coefficients take the values of $\phi^c = 0.1$, $\eta_{\text{theo}}^c = 0.301$, and $\eta_{\text{emp}}^c = 0.399$.

2.3. Square tube

The uncertainties in the geometry of the square-sectioned tube are also characterized by two random variables: the edge length C and the material thickness t_s. These values have been chosen so that both the circular and square tubes have the same values of cross-sectional area and wall cross-sectional area. This entails choosing a wall thickness $t_s = \sqrt{\pi}\, t_c/2$ and an edge length $C = \sqrt{\pi}\, D/2$, leading to a square tube with $C = 70.90$ mm and $t_s = 1.77$ mm as the baseline design. Moreover, these geometrical parameters lead to the asymmetric mode, which offers the highest specific energy absorption values. Table 3 presents the statistical moments considered for the variables studied.

Design		Standard deviation		
variable	Mean	COV = 2 %	COV = 5 %	COV = 10 %
C (mm)	70.90	1.418	3.545	7.090
t_s (mm)	1.77	0.0354	0.0885	0.177

Table 3: Statistical moments for the geometrical random design variables for the square tube.

To study the crashworthiness response of the tube, two formulas are used to estimate the average crushing force $P_{\text{s-mean}}$ and one for the peak force $P_{\text{s-max}}$. The empirical formula from Abramowicz and Jones [49] predicts $P_{\text{s-mean}}$ as

$$P_{\text{s-mean}}^{\text{emp}} = 38.12(C/t_s)^{1/3}M_0. \tag{8}$$

Moreover, the effective crushing distance of the tube shall be taken into account following the approach from Abramowicz [50], in which a factor will divide equation (8). For this particular baseline design it is found that the effective crushing distance is approximately 0.85 times the original tube length, thus the resulting empirical formula for predicting the average crushing force reads

$$P_{\text{s-mean}}^{\text{emp}} = 44.85(C/t_s)^{1/3}M_0. \tag{9}$$

Wierzbicki and Abramowicz [13] have also provided a theoretical formula for the average crushing force of polygonal tubes, reading

$$P_{\text{s-mean}}^{\text{theo}} = \frac{3n}{s} \sqrt[3]{2\pi\, I_1(\psi_0)I_3(\psi_0)}\; \sigma_0\, t_s^{5/3}\, C^{1/3}, \tag{10}$$

where n is the number of corners, ψ_0 is the angle between corners ($\psi_0 = \pi/4$ for the square tube), and I_i are coefficients particularized for each geometry. In the case of square sections, $I_1(\pi/4) = 0.58$ and $I_3(\pi/4) = 1.15$.

On the other hand, the peak crushing force is predicted through Timoshenko and Gere [51] as

$$P_{\text{s-max}}^{\text{theo}} = \left[k\frac{\pi^2\, E_r}{12(1-v_r^2)}\left(\frac{t_s}{C}\right)^2 + \sigma_c \right] A_S^s, \tag{11}$$

where k is the buckling coefficient taking the value of $k = 6.98$ for the considered boundary conditions, σ_c is calculated by

$$\sigma_c = \sigma_y \left[1 - \left(\frac{E_r}{E}\right)\left(\frac{1-v^2}{1-v_r^2}\right) \right], \tag{12}$$

with σ_y representing the material's yield stress, E_r being defined by

$$E_r = \frac{4EE_t}{\left(\sqrt{E} + \sqrt{E_t}\right)^2}, \tag{13}$$

$E_t = \partial\sigma/\partial\varepsilon$ being the tangent modulus, and $v_r = 0.5$.

The solitidy ratio and structural effectiveness are also quantified for the square tube, with the former being

$$\phi^s = \frac{A_S^s}{A_C^s} = \frac{4t_s\, C}{C^2} = \frac{4t_s}{C}, \tag{14}$$

while equation (9) can be transformed into

$$\eta_{\text{theo}}^s = 1.11(\phi^s)^{2/3}. \tag{15}$$

Thornton et al. [48] also provided the empirical prediction for the structural effectiveness of square tubes as

$$\eta_{\text{emp}}^c = 1.4(\phi^s)^{0.8}. \tag{16}$$

Particularized for this square tube, the coefficients take the values of $\phi^s = 0.1$, $\eta_{\text{theo}}^s = 0.239$, and $\eta_{\text{emp}}^s = 0.222$.

3. Numerical models

Uncertainty quantification of thin-walled members can also be estimated via numerical methods, constituting the only feasible approach in most complex structures without analytical solutions. For this case, finite element simulations replace equations (1) to (3) and (9) to (11), while sampling and surrogate modeling techniques circumvent their analytical error propagation.

3.1. Sampling and surrogate models

Surrogate-based methods replace an expensive and complex physical models by another physical or mathematical model, the surrogate- or meta-model, with the purpose of reducing the time required to evaluate the former. For this reason, the original objective functions f_i are replaced by other functions, $\hat{f}_i$, which are less costly to evaluate. This surrogate model is faster when computed as it is usually constructed with more tractable functions. These functions avoid the singular, discontinuous, and non-differentiable points from the original model. The similarity of the approximation between the real and surrogate models will condition the results obtained in a later phase.

The first step for obtaining the surrogate model consists in defining a sampling plan. This sampling is crucial, since the number of points chosen N_s will condition later on the suitability of the surrogate model. Although sampling techniques as full factorial sampling or Montecarlo methods are available, only the latin hypercube sampling (LHS) [52] from the LHS library [53] is used in this research. This stratified method creates a set of data points that have homogeneous projections onto each variable axis. The design space is split into equally-sized hypercubes, and points are placed into them so that no superimposed projections exist onto the variables' axes.

After the required data is retrieved from the sampling, the next step is the building process itself, which consists in adjusting the proper functions to the data points obtained. The code from the Surfpack library [54] is used for the construction and fitness assessment of the surrogate models. Four different strategies are considered throughout this research, as some surrogate models may yield better results depending on the sampling data trends and noise. Those techniques are the Gaussian process (Kriging) [55, 56], multivariate adaptive regression splines (MARS) with second-order interpolation and a maximum of 60 bases [57], polynomial response surfaces (PRS) with quadratic trend functions [58], and the moving least squares (MLS) method with third-order polynomials [59, 60].

After the surrogate is constructed, it needs to be established whether the surrogate model will produce reliable results and, additionally, how reliable. The suitability of the metamodel is determined through its trend functions, and in order to judge their accuracy, the goodness of fit R^2 is looked into. For the following research, it was established than surrogate models with a $R^2 \leqslant 0.98$ would not be accepted, as lower values would not provide confident results later on. However, this indicator is not useful for Gaussian processes as they have an error equal to zero in the sampling points, thus always yielding $R^2 = 1$.

In order to test the accuracy of the emulator, the mean absolute error (MAE) metric is also evaluated, although in some cases the sole evaluation of the error can guide towards misleading results. However, when the error is evaluated using a cross-validation strategy, the predictive capability of the surrogate comes into play, as different sets of the sampling data are progressively removed and compared to the fitness of the surrogate made from the complete sampling. Thus, the results from evaluating the R^2 or MAE indicators during cross-validation help identify metamodels with excessive noise and where the main trend is not well captured.

The numerical UQ performed in this research relies on the Abaqus 2017 [61] software for the finite element design, simulation, and post-processing of results; while the LHS library [53] is used for the sampling process and the Surfpack library [54] provides the code for the construction of the surrogate models.

3.2. Finite element analysis

For the numerical prediction of the selected metrics, non-linear finite element simulations are performed with the Abaqus 2017 commercial software with central difference explicit version. The details of the analyses and the post-processing of the data retrieved are now explained.

3.2.1. Impact simulation

The numerical simulation is performed by crushing the 25 centimeter-long thin-walled members between two rigid plates at a constant speed of $V_{imp} = 10$ m/s perpendicular to the cross-sectional plane ($\theta_{imp} = 90°$). However, variability in the impact conditions is considered similarly as the uncertainties in material and geometry, albeit these may only be analyzed via FEA. The statistical moments considered for the impact and angle speed normal distributions are found in table 4. Moreover, tangential friction coefficient of 0.2 and hard contact in the normal component are implemented as global interaction properties.

| Parameter | Mean | Standard deviation | | |
		COV = 2 %	COV = 5 %	COV = 10 %
V_{imp} (m/s)	10.0	0.2	0.5	1.0
θ_{imp} (°)	90.0	1.8	4.5	9.0

Table 4: Statistical moments for the impact random design variables for the FEA of both tubes.

Concerning the mesh, different element sizes were studied as to obtain the optimum trade-off between accuracy and computational requirements. The mesh sensitivity analysis from table 5 shows that the tube should be modeled with quadrilateral shell elements with reduced integration (denoted as S4R in Abaqus) and enhanced hourglass control, with edges approximately 3 millimeters long. This mesh size ensures a stable collapse of the tube of the circular and square tubes, with the same number of folds and similar absorbed energy obtained with finer meshes. The usage of solid elements for this parts is disregarded due

to the large number of elements required for the analysis and the consequently high computational cost. A front view of the baseline meshed models is presented in figures 1 and 2.

Size (mm)	Elements (number)	$P_{\text{c-mean}}^{\text{FEA}}$ (kN)	$P_{\text{c-max}}^{\text{FEA}}$ (kN)	Time (hh:mm)
6.0	1840	71.89	143.76	1:58
5.0	2668	72.27	142.68	3:02
4.0	4087	68.25	137.85	5:38
3.0	7090	65.91	134.04	10:50
2.0	15743	65.51	132.62	45:41
1.0	63118	65.49	132.11	292:42
Analytical	-	65.91	133.51	0:01

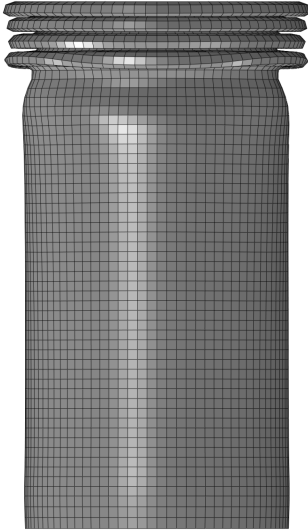Table 5: Mesh sensitivity analysis for baseline circular tube.

Figure 1: Finite element crushing simulation of circular tube after formation of four folds.

3.2.2. Post-process

The techniques used for obtaining the force-displacement curves and, consequently, average and peak force values, also have a noteworthy effect on the final results. After the completion of each simulation, a Python script automatically opens the results file and retrieves the unfiltered force-time data for the analysis. Later, this data undergoes a SAE 600 filter [62] as recommended by the literature [63], and is combined with displacement-time data for the final force-displacement output.

For the acquisition of the peak force, it is found that the unfiltered data predicts with higher resemblance the values provided by equation (3), with discrepancies reduced from 27.6% for the filtered value to 2.2% for the unfiltered. Figure 3 shows both response curves for the baseline circular design. Although it is not known whether the unfiltered or filtered values would better agree with experimental results, the authors deemed best the
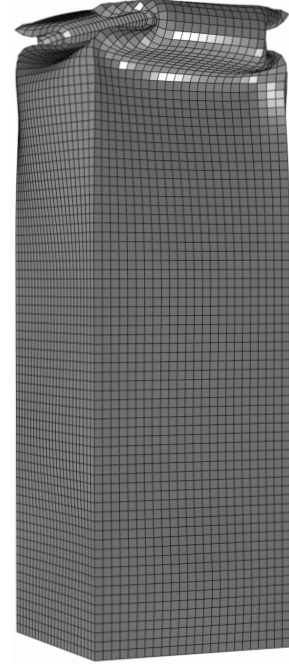

Figure 2: Finite element crushing simulation of square tube after formation of the first fold.

use of the unfiltered value for the sake of comparison between both the analytical and numerical procedures.

Moreover, the calculation of $P_{\text{mean}}^{\text{FEA}}$ is performed by two different methods. Initially, the average force is determined by the numerical integration of the area under the curve until a certain crushing distance is reached, which in this case was set to 150 millimeters. However, this entails considering the initial buckling force and not calculating the average force for an integer number of folds, which increases the error and variability of the studied metric. Thus, another post-processing scheme is developed in which $P_{\text{mean}}^{\text{FEA}}$ is calculated by disregarding the initial fold and its peak force, averaging it for a specified number of full folds (four full folds are selected for these calculations), increasing the robustness of the post-process and reducing noise for the studied metric. Figure 3 also offers a graphic depiction of the result for both aforementioned schemes, showing how the displacement scheme overestimates the analytical result for P_{mean}.

4. Results

The results from the error propagation of each uncertainty source are hereunder presented. First, the numerical uncertainties affecting both tubes are offered, while the operational and manufacturing uncertainty sources are separately considered for each of the tube geometries.

4.1. Numerical uncertainties

The results from the effect of numerical incertitudes, comprising a study of different surrogate models and the numerical noise from the finite element simulations is now detailed.
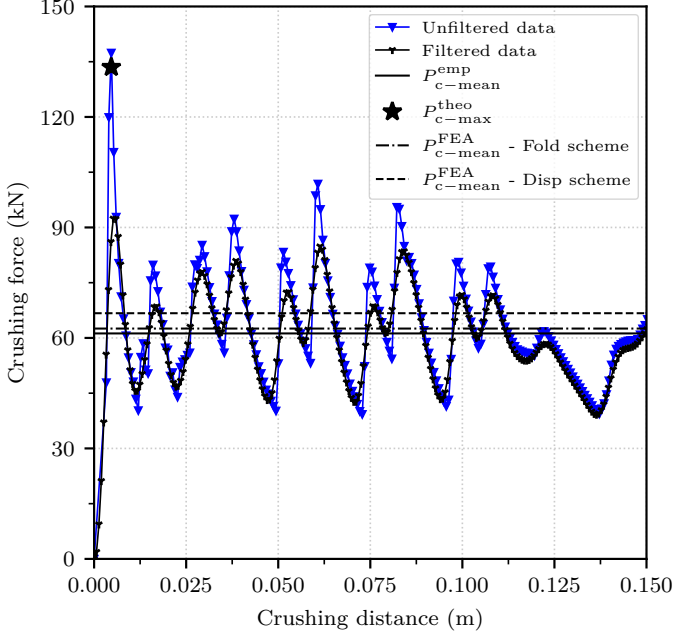
Figure 3: Comparison between average and peak crushing loads obtained from the analytical formulas in equations (1) and (3) and the numerical simulation with two post-processing schemes.

4.1.1. Surrogate performance

To analyze the performance of the surrogate models used and the number of samples required to accurately capture the values and trends of the metrics studied, different comparisons are run both with the analytical formulas and the finite element simulations. The results hereunder presented correspond to the circular tube with geometrical uncertainties (see table 2) with a COV = 5%, while the metrics are the average and peak loads obtained both from analytical formulas and the numerical simulation ($P_{\text{c-mean}}^{\text{emp}}$, $P_{\text{c-mean}}^{\text{FEA}}$, $P_{\text{c-max}}^{\text{theo}}$, and $P_{\text{c-max}}^{\text{FEA}}$).

First, all four metamodels are compared in terms of R^2 and the mean absolute error (MAE) with and without a 10-fold cross-validation scheme. Results from table 6, retrieved from 60 samples, show that the kriging metamodel outperforms the others for the analytical formulas, not only because of the $R^2 = 1$ inherent to Gaussian processes, but also for the reduced values of the MAE in both $P_{\text{c-mean}}^{\text{emp}}$ and $P_{\text{c-max}}^{\text{theo}}$. In the case of $P_{\text{c-mean}}^{\text{emp}}$, kriging's error is two magnitude orders smaller than that from other surrogates, while for $P_{\text{c-max}}^{\text{theo}}$ is one magnitude order smaller than MARS and within the same order as the MLS and PRS metamodels. However, it is important to note than MAE values, even after cross-validation, are less than 1% of the average value of the metrics, and $R^2 \geq 0.999$ for all four metamodels. The root mean squared error (RMSE) is also provided for all metamodels to further look into the capabilities of the surrogates and detect any inconsistencies with the MAE results. The values, included in table 6, confirm the validity of the models studied. Thus, and besides the superior approximation provided by kriging, all four metamodels can be deemed acceptable for accurately predicting $P_{\text{c-mean}}^{\text{emp}}$ and $P_{\text{c-max}}^{\text{theo}}$ with the considered number of samples.

Next, a similar procedure is performed but substituting the analytical formulas by the numerical responses $P_{\text{c-mean}}^{\text{FEA}}$ and $P_{\text{c-max}}^{\text{FEA}}$. A review of the results for the simulation data in table 6 now reveals that the worst fit is provided by kriging, which yields MAE values considerably higher than those from its counterparts. In this case, the MARS metamodel with 2nd-order base functions obtains a higher R^2 and the lowest MAE value of all four metamodels. Looking into the RMSE results, the MLS and MARS surrogates outperform those from kriging and the polynomials, with values under 1 kN for both of the metrics studied.

It is important to note than for this latter case, the metamodel has to accurately estimate the values at the sampling points as well as filtering-out the high-frequency noise from FEA's, which kriging fails to do as it is required to pass through all the sampling points provided. The other three metamodels overcome this on account of having an $R^2 < 1$ but better predicting the value of the function outside the sampling points. Equivalent tests as the one here described were carried out with different uncertainty parameters, COV's, and number of samples, all leading to similar conclusions in terms of surrogate performance. From within the four, and in view of the previous results, the MLS and MARS metamodels offer a better fit for the purpose of this research than PRS or kriging do. Moreover, and given the slight edge found of MARS over MLS surrogates, the former method is selected as the surrogate model of choice for the rest of the investigation.

Moreover, table 7 presents the evolution of $\text{E}\left[P_{\text{c-mean}}^{\text{emp}}\right]$ and $\sigma\left[P_{\text{c-mean}}^{\text{emp}}\right]$ with their 95% confidence intervals (CI) as the number of samples used for the metamodel construction is increased. The results, also depicted in figures 4a and 4b, show considerable noise for the predicted values of mean and standard deviation when the number of samples is below 30 or 40, with excessively large 95% CI ranges. Moreover, the software is not able to provide data for $\text{E}\left[P_{\text{c-max}}^{\text{theo}}\right]$ and $\sigma\left[P_{\text{c-max}}^{\text{theo}}\right]$ when the number of samples is below 12 as the number of points is deemed too low. However, as the number of points selected goes over 50, the average values stabilize with only small fluctuations observed; while the 95% CI tightens around the predicted value and is only slowly decreased after this point. When a similar procedure as the above described is performed for the square cross-section, homologous results are obtained. Thus, and also considering the trade-off between accuracy and computational efficiency, the selected number of samples for the MARS metamodels used is that of 60.

Furthermore, and considering the stochastic nature of the LHS scheme, different seed values were used during the sampling as to assess their effect on the MARS surrogate model accuracy. Results showed that when using 60 samples variations in the metamodels' R^2, MAE, and RMSE were less than 2% regardless of the seed value used, which was deemed of a minor effect for the purpose of this research, consequently using a fixed seed value throughout the rest of the investigation. There also exist prediction uncertainties inherent to the use of surrogate modeling, which although negligible in the case of the

	Model	$P_{\text{c-mean}}$			$P_{\text{c-max}}$		
		R^2	RMSE (kN)	MAE (kN)	R^2	RMSE (kN)	MAE (kN)
Analyt.	Krig	1.000	$2.323 \cdot 10^{-2}$	$5.302 \cdot 10^{-2}$	1.000	$3.008 \cdot 10^{-2}$	$2.758 \cdot 10^{-2}$
	MARS	≥ 0.999	$3.803 \cdot 10^{-2}$	$5.558 \cdot 10^{-3}$	≥ 0.999	$3.388 \cdot 10^{-2}$	$9.847 \cdot 10^{-4}$
	MLS	≥ 0.999	$9.865 \cdot 10^{-2}$	$1.385 \cdot 10^{-3}$	≥ 0.999	$2.255 \cdot 10^{-2}$	$2.497 \cdot 10^{-5}$
	PRS	≥ 0.999	$1.006 \cdot 10^{-1}$	$2.494 \cdot 10^{-3}$	≥ 0.999	$2.740 \cdot 10^{-1}$	$2.406 \cdot 10^{-5}$
Simul.	Krig	-	1.702	1.770	-	1.918	1.405
	MARS	0.985	0.998	0.652	0.997	0.501	0.897
	MLS	0.952	0.956	0.736	0.987	0.911	0.904
	PRS	0.934	1.314	1.065	0.986	1.108	0.963

Table 6: Comparison of metamodel performance for $P_{\text{c-mean}}^{\text{emp}}$, $P_{\text{c-max}}^{\text{theo}}$, $P_{\text{c-mean}}^{\text{FEA}}$, and $P_{\text{c-max}}^{\text{FEA}}$ of a circular tube with geometrical uncertainties (COV = 5%, 60 samples). Mean absolute error (MAE) results correspond to values with 10-fold cross-validation.

metamodels from the analytical formulas given the high values of the fitness metrics studied, they could significantly contribute to incertitudes when metamodels stem from numerical simulations [64, 65]. However, the account of such effect has been also disregarded for this particular metamodels considering that the MARS metamodels also yields $R^2 > 0.985$ for both metrics studied.

4.1.2. Numerical noise

Numerical noise in FEA is also a source of error in uncertainty propagation. Following a similar approach to that of Gilkeson et al. [43], this investigation will also attempt to quantify the oscillation frequency (measuring whether the function behaves monotonically or there are gradient changes between each point) and standard deviation of the numerical responses. The baseline circular tube is chosen, allowing the thickness to vary between 1.5 mm $\leq t_c \leq$ 2.5 mm, while disregarding variations in the diameter as this would slightly change the mesh definition and introduce further sources of noise.

As a benchmark for the FEA, the analytical formulas are first used for the average force $P_{\text{c-mean}}^{\text{emp}}$ and the peak force $P_{\text{c-max}}^{\text{theo}}$. Then, an homologous procedure is repeated with the numerical counterparts $P_{\text{c-mean}}^{\text{FEA}}$ and $P_{\text{c-max}}^{\text{FEA}}$, with the former being retrieved through both schemes described in section 3.2.2. Figures 5 and 7 offer the comparison between the analytical and numerical responses as the plate thickness progressively increases, easily distinguishing the results from the simulation by their fluctuations around the analytical values.

Moreover, these results are normalized with respect to the tube's thickness, dividing the results by a constant and the tube's thickness raised to a power, which leads to $\overline{P}_{\text{c-mean}} = P_{\text{c-mean}}/\left(\beta_1 t_c^{1.68}\right)$ and $\overline{P}_{\text{c-max}} = P_{\text{c-max}}/\left(\beta_2 t_c^2\right)$, where β_1 and β_2 are the constants that normalize equations (1) and (3). These techniques allow the characterization of noise as represented in figures 6 and 8.

The results for the analytical values in table 8 show a perfect fit, yielding a constant value of $\overline{P}_{\text{c-mean}}^{\text{theo}} = \overline{P}_{\text{c-max}}^{\text{theo}} = 1$ for both metrics, while those from the FEA offer relevant values of noise. When comparing both post-process schemes for obtaining $P_{\text{c-mean}}^{\text{FEA}}$, the fold scheme has a slight advantage with better resemblance with the empirical results, a smaller standard de-

viation, and nearly half the oscillation frequency. This high oscillation frequency can constitute a hindering factor during the construction of most surrogate models, specially true for Gaussian processes which are required to pass through all the sampling points. Moreover, the breadth of $A_{3\sigma}$ (the area of the 95% CI) is just over 6.5% for the fold-scheme, while the integration of $P_{\text{c-mean}}^{\text{FEA}}$ by means of a constant displacement leads to an $A_{3\sigma}$ of nearly 8%. Thus, the fold-scheme is selected for the rest of this investigation.

The performance of $\overline{P}_{\text{c-max}}^{\text{FEA}}$ is also evaluated, yielding an oscillation frequency of 40%. Furthermore, the average fit of this metric within the studied thickness range is nearly that of the analytical results, although a closer look at figure 8 reveals how values are slightly under-predicted for thickness below 1.85 mm, and over-predicted after that value. However, the area of the 95% CI for this metric is under 9%, considered an acceptable value given the non-linear and dynamic nature of these simulations. Moreover, similar results are obtained when an homologous procedure is repeated for the square cross-section, with the the fold-scheme post-process also delivering a better performance of $P_{\text{s-mean}}^{\text{FEA}}$ and the unfiltered data offering a closer match between $P_{\text{s-max}}^{\text{FEA}}$ and $P_{\text{s-max}}^{\text{theo}}$.

4.2. Circular tube

In this section, the propagation of geometrical, material, and impact uncertainties on the axially-loaded circular tube is presented.

4.2.1. Geometrical uncertainties

First, the diameter and plate thickness of the tube are assumed to be defined by a normal distribution with three different coefficients of variation. The propagation of variables is to be performed with both combined, studying its effect on the mean and peak crushing loads.

In the results presented in table 9, it is first seen that the mean value for $P_{\text{c-mean}}^{\text{emp}}$ resulting from the statistical propagation and the surrogate model is matched to the second decimal place, although minor discrepancies in the standard deviation are observed overshooting the value by 1% to 3%. This is considered an acceptable error for the purposes here intended, although it could be reduced by increasing the sampling size.

8

| Samples	$\mathrm{E}\left[P_{\text{c-mean}}^{\text{emp}}\right] \pm 95\%\text{CI}$	$\sigma\left[P_{\text{c-mean}}^{\text{emp}}\right] \pm 95\%\text{CI}$	$\mathrm{E}\left[P_{\text{c-max}}^{\text{theo}}\right] \pm 95\%\text{CI}$	$\sigma\left[P_{\text{c-max}}^{\text{theo}}\right] \pm 95\%\text{CI}$
6	66.62 ± 7.77	7.40 ± 6.76	-	-
8	66.01 ± 4.86	5.81 ± 3.99	-	-
10	66.18 ± 4.25	5.94 ± 3.38	-	-
12	66.03 ± 3.45	5.43 ± 2.69	134.25 ± 5.77	9.08 ± 4.49
15	66.12 ± 3.18	5.75 ± 2.43	134.41 ± 5.38	9.71 ± 4.10
20	66.19 ± 2.84	6.07 ± 2.13	134.48 ± 4.96	10.61 ± 3.71
30	66.02 ± 2.09	5.59 ± 1.53	134.18 ± 3.62	9.71 ± 2.66
40	66.01 ± 1.81	5.66 ± 1.32	134.15 ± 3.14	9.82 ± 2.28
60	65.91 ± 1.50	5.79 ± 1.08	134.16 ± 2.54	9.84 ± 1.83
80	65.95 ± 1.26	5.68 ± 0.91	134.12 ± 2.13	9.56 ± 1.52
100	66.01 ± 1.12	5.63 ± 0.80	134.18 ± 1.93	9.70 ± 1.38
250	65.98 ± 0.71	5.67 ± 0.50	134.13 ± 1.20	9.67 ± 0.86

Table 7: Evolution of MARS metamodel estimation for the mean and standard deviation values of $P_{\text{c-mean}}^{\text{emp}}$ and $P_{\text{c-max}}^{\text{theo}}$ and their 95% confidence intervals (CI) of a circular tube with geometrical uncertainties (COV = 5%). All values in kN.

Metric	$\overline{P}_{\text{c-mean}}^{\text{emp}}$	$\overline{P}_{\text{c-max}}^{\text{theo}}$	$\overline{P}_{\text{c-mean}}^{\text{FEA}}$ (folds)	$\overline{P}_{\text{c-mean}}^{\text{FEA}}$ (disp)	$\overline{P}_{\text{c-max}}^{\text{FEA}}$
Mean (kN)	1.000	1.000	0.979	0.974	0.999
Std (kN)	0.0	0.0	0.0219	0.0264	0.0297
Osc. freq (%)	0.0	0.0	32.5	60.0	40.0
A_σ (%)	0.0	0.0	2.19	2.64	2.97
$A_{3\sigma}$ (%)	0.0	0.0	6.57	7.95	8.92

Table 8: Statistical moments and numerical noise quantification [43] for normalized $\overline{P}_{\text{c-mean}}$ and $\overline{P}_{\text{c-max}}$ for the circular tube with analytical results and FEA after both post-process schemes. Results based on 40 samples.
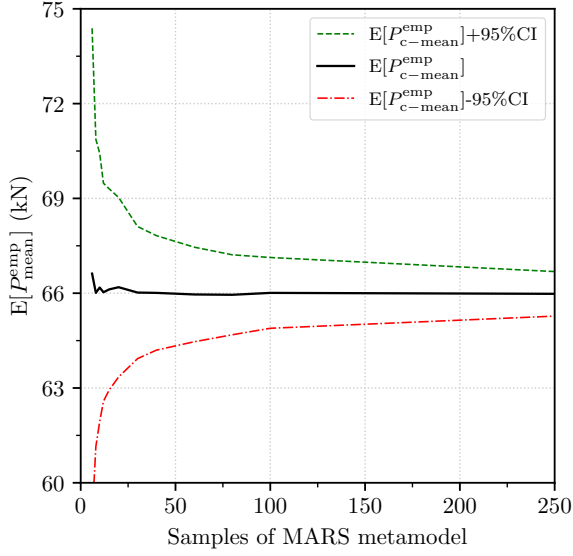
(a) Evolution of mean value for $P_{\text{c-mean}}^{\text{emp}}$ with number of samples used.
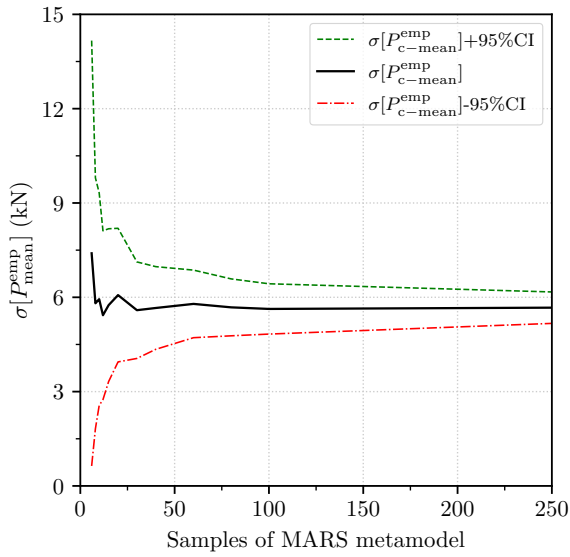
(b) Evolution of standard deviation for $P_{\text{c-mean}}^{\text{emp}}$ with number of samples used.

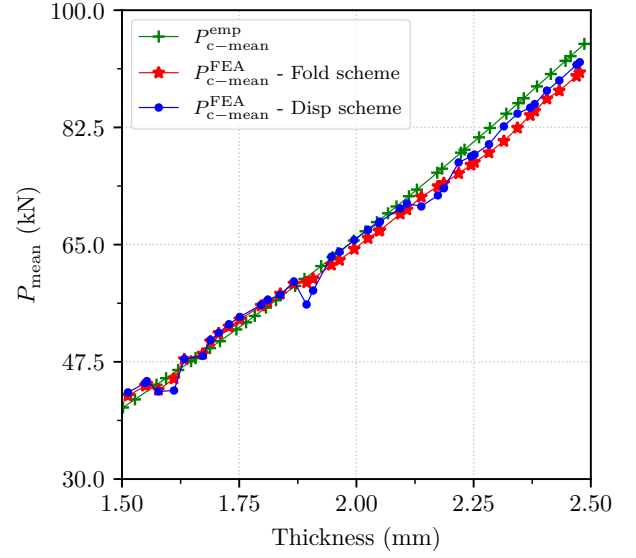Figure 4: Evolution of statistical moments for $P_{\text{c-mean}}^{\text{emp}}$ with number of samples used for the MARS metamodel.

Figure 5: Evolution of $P_{\text{c-mean}}^{\text{emp}}$ and $P_{\text{c-mean}}^{\text{FEA}}$ due to thickness variation. Results from equation (1) and FEA with the two postprocess schemes. Results based on 40 samples.

Figure 6: Evolution of normalized $\overline{P}_{\text{c-mean}}^{\text{emp}}$ and $\overline{P}_{\text{c-mean}}^{\text{FEA}}$ due to thickness variation. Results from equation (1) and FEA with the two postprocess schemes. Results based on 40 samples.
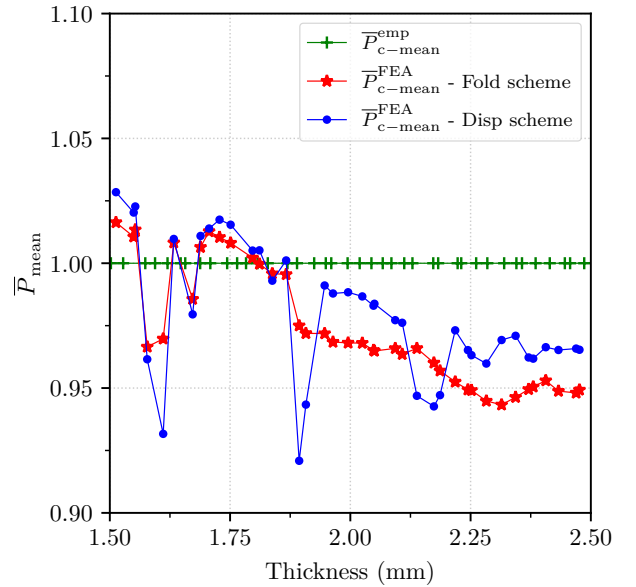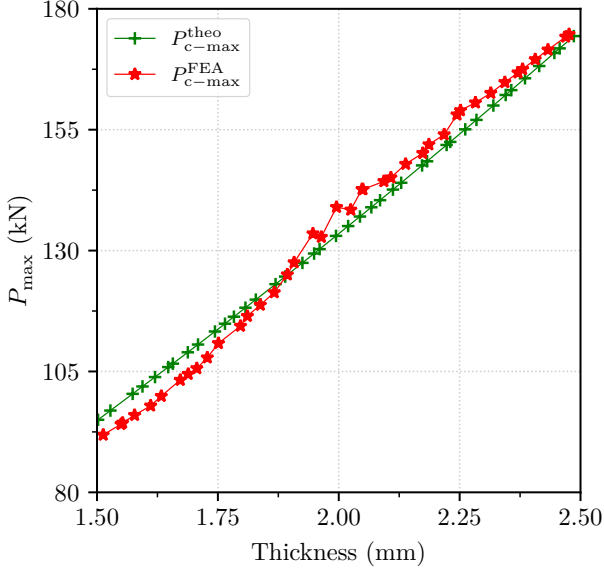
Figure 7: Evolution of $P_{\text{c-max}}^{\text{theo}}$ and $P_{\text{c-max}}^{\text{FEA}}$ due to thickness variation. Results from equation (3) and FEA. Results based on 40 samples.
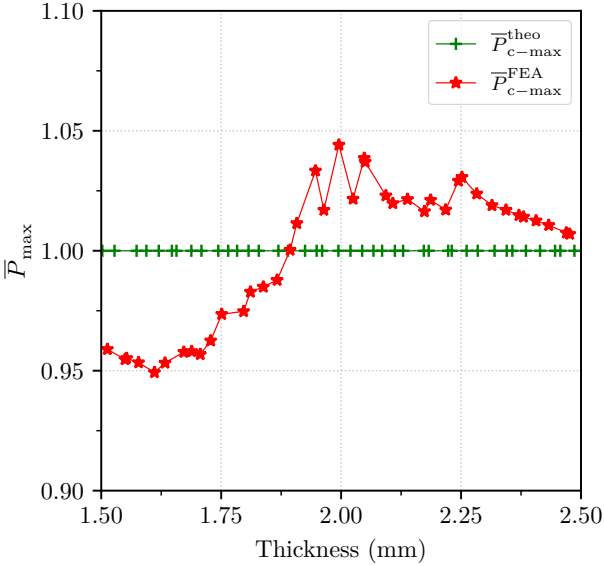
Figure 8: Evolution of normalized $\overline{P}_{\text{c-max}}^{\text{theo}}$ and $\overline{P}_{\text{c-max}}^{\text{FEA}}$ due to thickness variation. Results from equation (3) and FEA. Results based on 40 samples.

Among the three metrics studied, $P_{\text{c-max}}^{\text{theo}}$ has the smallest COV resulting values, while the results from $P_{\text{c-mean}}^{\text{emp}}$ and $P_{\text{c-mean}}^{\text{theo}}$ are fairly similar. Overall, the COV of the resulting metric after the combination of two uncertainty sources is increased less than 50% of the original COV value.

Uncertainty propagation is also performed with the two metrics retrieved from the FEA. When comparing the expected values for $P_{\text{c-mean}}^{\text{emp}}$ and $P_{\text{c-mean}}^{\text{FEA}}$, the difference is less than 0.1%, while the variation between analytical and numerical peak crushing loads is around 1%. The propagation based on numerical simulations also yields similar COVs than the analytical formulas, which are progressively reduced for both the mean and peak crushing forces as the COV of the variables is increased.

4.2.2. Material uncertainties

The uncertainty propagation procedure is repeated with material variability and presented in table 10, obtaining similar discrepancies in the expected value of the metrics between the numerical and analytical methods. However, since $P_{\text{c-mean}}^{\text{emp}}$ and $P_{\text{c-mean}}^{\text{theo}}$ from equations (1) and (2) are independent of E, the resulting standard deviations and COVs obtained from the analytical and metamodel propagation match almost perfectly the COV from the σ_0 variable. In the case of $P_{\text{c-max}}^{\text{theo}}$, which is influenced by both variables, the resulting variance is around 15% lower than that of a single variable.

Finally, the results from FEAs also show differences from mean values under 0.1% and 1% for average and peak crushing loads respectively. The propagation based on numerical simulations also yields lower COVs than the analytical formulas, which can be up to half of those for mean crushing forces and around 15% for the $P_{\text{c-max}}$.

4.2.3. Impact conditions uncertainties

The uncertainty quantification for circular tubes finalizes with variations in impact conditions. This is only studied here with the metamodels from numerical simulations rather than using the analytical formulas, as no analytical formulas are available for this purpose. The results in table 11 show how the expected value of $P_{\text{c-mean}}^{\text{FEA}}$ decreases around 1.5% with respect to that obtained from the previous uncertainty propagation. The evolution of the standard deviations and COVs, however, offer a peculiar behavior in which the COV is increased from 2% in the variables to 2.65% in the resulting metric, while it decreases from 10% to 6.82% in the latest case. This can be explained by a higher sensitivity of the responses when varying close to the average value, while being of a lesser effect as the variables take values further from the average.

On the other hand, the evolution of the standard deviations of $P_{\text{c-max}}^{\text{FEA}}$ presents the opposite behavior, increasing the COV of the resulting metrics as the standard deviation of the variables increases. A similar under-prediction in the average value of $P_{\text{c-max}}^{\text{FEA}}$ is also found, with an estimation 16% lower than the expected force.

4.3. Square tube

Now, the homologous uncertainty propagation procedures used with the circular tube are applied to the square-sectioned

		Mean	Standard deviation		
			COV = 2 %	COV = 5 %	COV = 10 %
Variables	D (mm)	80.00	1.60	4.00	8.00
	t_{c} (mm)	2.00	0.04	0.10	0.20
Analytical (stat)	$P_{\text{c-mean}}^{\text{emp}}$ (kN)	65.91	2.25 (3.41%)	5.64 (8.56%)	11.29 (17.13%)
Analytical (surr)	$P_{\text{c-mean}}^{\text{emp}}$ (kN)	65.91	2.32 (3.52%)	5.78 (8.77 %)	11.55 (17.52 %)
	$P_{\text{c-mean}}^{\text{theo}}$ (kN)	63.50	2.16 (3.40%)	5.39 (8.49%)	10.76 (16.94%)
	$P_{\text{c-max}}^{\text{theo}}$ (kN)	134.16	4.00 (2.92%)	9.84 (7.34%)	19.83 (14.61%)
Simulation	$P_{\text{c-mean}}^{\text{FEA}}$ (kN)	65.85	2.33 (3.54%)	5.33 (8.09%)	9.98 (15.16%)
	$P_{\text{c-max}}^{\text{FEA}}$ (kN)	135.76	4.13 (3.04%)	9.42 (6.94%)	18.31 (13.49%)

Table 9: Statistical moments for the geometrical design parameters and studied analytical metrics for the circular tube with three different COV. Values in brackets correspond to resulting COV for the metrics.

		Mean	Standard deviation		
			COV = 2 %	COV = 5 %	COV = 10 %
Variables	E (GPa)	73.10	1.462	3.655	7.310
	σ_0 (MPa)	280.00	5.60	14.00	28.00
Analytical (stat)	$P_{\text{c-mean}}^{\text{emp}}$ (kN)	65.91	1.32 (2.00%)	3.30 (5.00%)	6.59 (10.00%)
Analytical (surr)	$P_{\text{c-mean}}^{\text{emp}}$ (kN)	65.92	1.32 (2.00%)	3.29 (4.99%)	6.59 (10.00%)
	$P_{\text{c-mean}}^{\text{theo}}$ (kN)	63.50	1.27 (2.00%)	3.17 (4.99%)	6.35 (10.00%)
	$P_{\text{c-max}}^{\text{theo}}$ (kN)	134.04	2.21 (1.64%)	5.52 (4.12%)	11.09 (8.27%)
Simulation	$P_{\text{c-mean}}^{\text{FEA}}$ (kN)	65.89	0.60 (0.91%)	1.52 (2.31%)	2.96 (4.49%)
	$P_{\text{c-max}}^{\text{FEA}}$ (kN)	135.76	1.91 (1.41%)	4.04 (2.98%)	10.31 (7.59%)

Table 10: Statistical moments for the material design parameters and studied analytical metrics for the circular tube with three different COV. Values in brackets correspond to resulting COV for the metrics.

		Mean	Standard deviation		
			COV = 2 %	COV = 5 %	COV = 10 %
Variables	V (m/s)	0.2	0.004	0.01	0.02
	θ_{imp} (Degrees)	90	1.8	4.5	9.0
Simulation	$P_{\text{c-mean}}^{\text{FEA}}$ (kN)	64.94	1.72 (2.65%)	3.09 (4.75%)	4.42 (6.82%)
	$P_{\text{c-max}}^{\text{FEA}}$ (kN)	113.83	15.38 (13.51%)	35.81 (31.46%)	84.75 (74.45%)

Table 11: Statistical moments for the impact design parameters and studied analytical metrics for the circular tube with three different COV. Values in brackets correspond to resulting COV for the metrics.

component.

4.3.1. Geometrical uncertainties

The comparison of the mean predictions for $P_{\text{s-mean}}$ presented in table 12 shows almost equal values between the numerical and analytical results, with the those from the FEA being 1% lower than the empirical formula. Moreover, the usage of surrogate models induces a similar error in the calculation of the standard deviations of $P_{\text{s-mean}}^{\text{emp}}$ and $P_{\text{s-mean}}^{\text{theo}}$ as with the circular tube, overpredicting the moment by 0.7% to 1%. This is kept consistent for the three COV studied and both mean crushing force formulas.

In the case of $P_{\text{s-max}}$, the difference between the average values is more significant than with the circular tube with the analytical surrogate yielding a value 8.5% higher than the numerical simulation, although this can be attributed to a uniform disparity between the results of both predictions. When looking at the standard deviations, however, it is clear that dispersion from the metamodel from FEAs is notably lower, leading to COVs in the resulting metrics up to 55% lower than the ones provided from the analytical formulas.

4.3.2. Material uncertainties

The study of material uncertainties for the square tube reveals a similar behavior as its examination with the circular counterpart. Both analytical equations for $P_{\text{s-mean}}$ are independent of the Young's modulus, thus leading to matching COVs between σ_0 and $P_{\text{s-mean}}$ as shown in table 13. However, $P_{\text{s-max}}^{\text{theo}}$ does consider both variables for its calculation, increasing the COV of the results by less than 50% of the variables' COV.

The analysis of the simulation results, in which both variables affect the result metrics, offers similar mean values as those stemming from geometrical uncertainties, where the average crushing force almost matches $P_{\text{s-mean}}^{\text{emp}}$ and $P_{\text{s-max}}^{\text{FEA}}$ is 8.5% lower than the prediction from the formula. For the standard deviations and their respective COVs, the metamodel from FEAs performs better in the estimation of the average crushing load, reducing the COV by approximately 50% from the analytical solutions. In the case of the peak crushing force, however, the standard deviations and COVs are higher when computed with numerical simulation as a consequence of being metric with higher fluctuations and more prone to numerical noise.

4.3.3. Impact conditions uncertainties

The last of the uncertainty propagation results is carried out by using the impact angle and velocity as variables. These results, obtained only from numerical simulations and presented in table 14, manifest mean values 3.5% higher for $P_{\text{s-mean}}^{\text{FEA}}$ and around 15% lower for $P_{\text{s-max}}^{\text{FEA}}$. As with the circular tube, it becomes apparent that the effect of impact angle variations leads to a significant consequence on the peak force results. Still, in the case of the average value, this seems to be of a minor effect, with COVs for $P_{\text{s-mean}}^{\text{FEA}}$ being reduced by as much as to a fourth of the variables' COV.

To further understand the effect of the impact angle on the tube's response, figure 9 contains the force-displacement graphs for the square baseline tube where the impact angle is gradually

decreased from 90 to 80 degrees. In the comparison it is easily perceived how by only reducing the angle by 2 degrees, the peak force is decreased from 127.9 kN to 65.2 kN, nearly half of the original value. As the impact angle is further reduced, the $P_{\text{s-max}}^{\text{FEA}}$ now is lowered at a smaller rate, hitting a values around 50-55 kN when the angle reaches 82 degrees. This significant non-linear behavior of the studied metric explain the values for $P_{\text{s-max}}^{\text{FEA}}$ obtained in table 14, both in the reduced mean value and the high standard deviations with all three COVs. Per contra, $P_{\text{s-mean}}^{\text{FEA}}$ suffers an antagonistic comportment to the peak force, as its expected value is increased by 3.5% and the resulting COV is that of 2.32% even with a variables' COV of 10%. In this case, the variations in impact angle which severely affected the peak force at the beginning of the crushing process, do not have a major effect on the rest of the response in terms of average load. In figure 9 it is clearly seen how after the initial 10 mm of crushing the curves all follow a similar trend, and even the lower impact angles can yield higher loads in some parts of the crushing process.
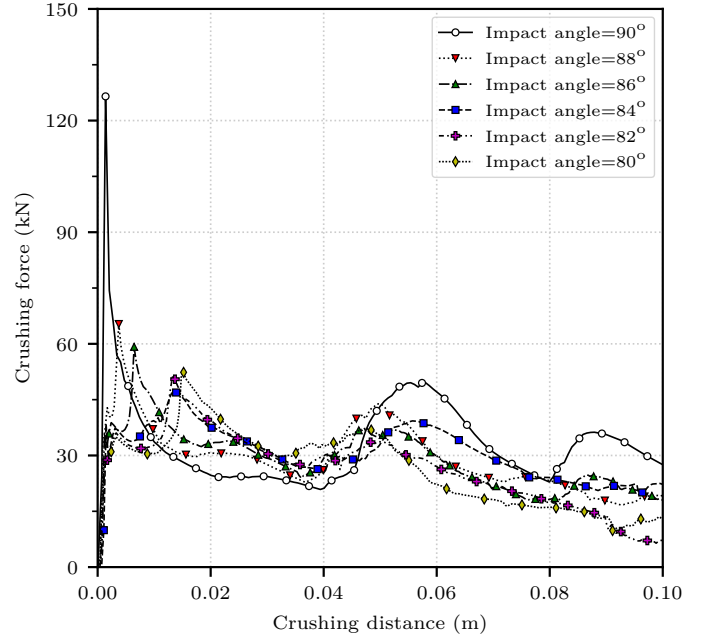

Figure 9: Force - displacement curves of baseline square tube crushed with different impact angles.

4.4. Tube comparison

The tubes' geometries were selected so that both cross-sections have the same solidity ratio, in this case $\phi^c = \phi^s = 0.1$. When this condition is met, the following is also true:

$$\frac{\eta^c}{\eta^s} = \frac{P_{\text{c-mean}}}{P_{\text{s-mean}}} \tag{17}$$

This equality, applied to the empirical formulas, which provide the best agreement with the simulations, is nearly achieved with $\eta_{\text{emp}}^c/\eta_{\text{emp}}^s = 1.81$ and $P_{\text{c-mean}}^{\text{emp}}/P_{\text{s-mean}}^{\text{emp}} = 1.88$, confirming a slight but acceptable error in the predictions.

13

		Mean	Standard deviation		
			COV = 2 %	COV = 5 %	COV = 10 %
Variables	C (mm)	70.90	1.418	3.545	7.090
	t_s (mm)	1.77	0.0354	0.0885	0.177
Analytical (stat)	$P_\text{s-mean}^\text{emp}$ (kN)	33.65	1.14 (3.40%)	2.86 (8.50%)	5.73 (17.02%)
	$P_\text{s-mean}^\text{theo}$ (kN)	29.04	0.99 (3.40%)	2.47 (8.50%)	4.94 (17.02%)
Analytical (surr)	$P_\text{s-mean}^\text{emp}$ (kN)	33.66	1.16 (3.44%)	2.89 (8.59%)	5.77 (17.14%)
	$P_\text{s-mean}^\text{theo}$ (kN)	29.04	1.00 (3.44%)	2.50 (8.61%)	4.99 (17.18%)
	$P_\text{s-max}^\text{theo}$ (kN)	139.94	9.91 (7.08%)	24.93 (17.81%)	51.21 (36.59%)
Simulation	$P_\text{s-mean}^\text{FEA}$ (kN)	33.32	2.02 (6.06%)	4.02 (12.06%)	6.01 (18.03%)
	$P_\text{s-max}^\text{FEA}$ (kN)	127.91	3.86 (3.02%)	9.04 (7.07%)	20.70 (16.18%)

Table 12: Statistical moments for the material parameters and studied analytical metrics for the square tube with three different COV. Values in brackets correspond to resulting COV for the metrics.

		Mean	Standard deviation		
			COV = 2 %	COV = 5 %	COV = 10 %
Variables	E (GPa)	73.10	1.462	3.655	7.310
	σ_0 (MPa)	280.00	5.60	14.00	28.00
Analytical (stat)	$P_\text{s-mean}^\text{emp}$ (kN)	33.65	0.67 (2.00%)	1.68 (5.00%)	3.37 (10.00%)
	$P_\text{s-mean}^\text{theo}$ (kN)	29.04	0.58 (2.00%)	1.45 (5.00%)	2.90 (10.00%)
Analytical (surr)	$P_\text{s-mean}^\text{emp}$ (kN)	33.65	0.67 (2.00%)	1.68 (5.00%)	3.36 (9.99%)
	$P_\text{s-mean}^\text{theo}$ (kN)	29.04	0.58 (2.00%)	1.45 (5.00%)	2.90 (10.00%)
	$P_\text{s-max}^\text{theo}$ (kN)	139.94	3.86 (2.76%)	9.72 (6.95%)	19.80 (14.15%)
Simulation	$P_\text{s-mean}^\text{FEA}$ (kN)	33.32	0.28 (0.84%)	1.11 (3.33%)	1.67 (5.01%)
	$P_\text{s-max}^\text{FEA}$ (kN)	127.91	4.78 (3.74%)	12.09 (9.45%)	19.01 (14.86%)

Table 13: Statistical moments for the material design parameters and studied analytical metrics for the square tube with three different COV. Values in brackets correspond to resulting COV for the metrics.

		Mean	Standard deviation		
			COV = 2 %	COV = 5 %	COV = 10 %
Variables	V (m/s)	0.2	0.004	0.01	0.02
	θ_imp (Degrees)	90	1.8	4.5	9.0
Simulation	$P_\text{s-mean}^\text{FEA}$ (kN)	34.50	0.43 (1.25%)	0.44 (1.28%)	0.80 (2.32%)
	$P_\text{s-max}^\text{FEA}$ (kN)	108.72	12.01 (11.05%)	17.04 (15.67%)	58.55 (53.85%)

Table 14: Statistical moments for the impact design parameters and studied analytical metrics for the square tube with three different COV. Values in brackets correspond to resulting COV for the metrics.

The efficiency of both configurations is also compared in terms of the energy-absorbing effectiveness factor ψ, defined as the ratio between the elastic and plastic strain energy absorbed by a structure, and the energy absorbed in the same volume of material up to failure in tension [66, 67]. This energy-absorbing effectiveness factor can be written as

$$\psi = \frac{\int_0^{\delta_f} P \, d\delta}{V \int_0^{\epsilon_f} \sigma \, d\epsilon} = \frac{P_{\text{mean}} \, \delta_f}{\sigma_0 \, A_C \, L \, \epsilon_f}, \tag{18}$$

where P is the axial crushing force and δ the crushing distance, comprised between 0 and the final value δ_f, with $\delta_f \approx 0.75L$. In the denominator, V represents the volume of material of the specimen, while σ is the tensile stress, and ϵ and ϵ_f are the uniaxial engineering strain and rupture strain respectively. According to equation (18), the effectiveness factor for the circular tube is $\psi_c = 1.61$, whereas the square tube yields a $\psi_s = 0.83$, leading to this circular section being nearly twice as efficient as the square counterpart.

When looking at the results from the uncertainty propagation of both designs there seem to be some common behaviors, specially in the case of geometric uncertainties. Two simple correlation matrices for both designs are presented in tables 15 and 16, respectively obtained from the surrogate models of the analytical formulas and the numerical simulations. Both analyses show that the plate thickness of the tubes has the greatest effect on both metrics, with coefficients ranging between 0.81 and 0.97. The diameter and length have a smaller impact, with a correlation coefficient around 0.2 for average crushing loads and a higher value of approximately 0.55 for the peak force. However, the sensitivity analysis from numerical simulations of the material uncertainties hints that both tubes are affected from those in the opposite manner, as the elastic modulus has the greatest effect on the metrics for the square section, while flow stress values reach correlation values over 0.93 with the functions studied for circular tube. Moreover, this is ratified when looking at the results from table 15, except in the response of $P_{\text{s-mean}}$ which is mostly dependent on the variations of the flow stress rather than the elastic modulus. Finally, correlation values for the impact variables (only studied from numerical simulations) are mostly below 0.1 and even take negative values, in concordance with the results previously presented in tables 11 and 14. An exception is found in the case of the circular tube, where impact velocity and angle have a correlation coefficient with the resulting average load of approximately 0.85 and 0.22 respectively.

5. Conclusions

In the research described in this paper, the analytical and numerical crashworthiness uncertainty quantification of two aluminum thin-walled energy absorbers is performed, considering the average and peak crushing loads as metrics. Three different approaches are followed: a statistical error propagation of the analytical formulas, the UQ from a surrogate model from the

Variable	P_{mean}		P_{max}	
	$P_{\text{c-mean}}^{\text{emp}}$	$P_{\text{s-mean}}^{\text{emp}}$	$P_{\text{c-max}}^{\text{theo}}$	$P_{\text{s-max}}^{\text{theo}}$
D / C	0.220	0.292	0.513	0.323
t_c / t_s	0.982	0.980	0.845	0.931
E	0.036	0.036	0.298	0.999
σ_0	1.000	1.000	0.965	0.034

Table 15: Simple correlation matrix between variables and response metrics for the circular and square tubes. Results obtained for the MARS surrogate from the analytical formulas, with 60 sampling points and COV = 5%

Variable	P_{mean}		P_{max}	
	$P_{\text{c-mean}}^{\text{FEA}}$	$P_{\text{s-mean}}^{\text{FEA}}$	$P_{\text{c-max}}^{\text{FEA}}$	$P_{\text{s-max}}^{\text{FEA}}$
D / C	0.218	0.227	0.558	0.541
t_c / t_s	0.978	0.813	0.939	0.934
E	0.302	0.860	0.263	0.687
σ_0	0.952	-0.062	0.937	0.599
V	0.856	0.019	0.032	-0.264
θ_{imp}	0.218	0.071	-0.071	-0.045

Table 16: Simple correlation matrix between variables and response metrics for the circular and square tubes. Results obtained for the MARS surrogate from the numerical simulations, with 60 sampling points and COV = 5%

15

formulas, and from a surrogate model built from finite element simulations. The following conclusions can be withdrawn:

- The performance comparison between the four metamodels studied shows that MARS outperforms the others when stemming from numerical simulations, while offering similar R^2 to the other in the case of analytical formulas. A study on sample size returns similar mean values as with statistical propagation and a standard deviation overshot between 1% and 3% when 60 or more samples are used.

- Numerical noise from the simulations displays an oscillation frequency below 40% for both metrics, while $A_{3\sigma}$ is approximately 6.5% and 9% for the average and peak crushing loads respectively. It is shown that the effects of this noise can be mitigated with enough samples, the selection of the appropriate surrogate model, and a post-processing scheme based on the number of folds developed rather than on a fixed crushing distance.

- The use of properly adjusted numerical simulations can accurately match the results from the analytical formulas when calculating the statistical moments during the UQ process. The circular tube offers a slightly better agreement with the formulas than the square counterpart.

- Both tube configurations are similarly affected from the geometric uncertainties, where plate thickness is more influential on the results than diameter or edge length. In the case of material uncertainties, the elastic modulus is the most influential variable for the square section, whereas the equivalent flow stress has the highest correlation with the metrics from the circular tube.

- Uncertainties in the impact conditions can only be studied via metamodels constructed from numerical simulations. The average crushing load can be retrieved with an acceptable accuracy, where the square section proves to be more robust than the circular. Peak load values rapidly decrease when the impact angle varies from a perfect axial collision, leading to reduced mean values and high standard deviations after the error propagation.

References

[1] C. Bisagni, Crashworthiness of helicopter subfloor structures, International Journal of Impact Engineering 27 (2002) 1067–1082.

[2] J. Paz, J. Díaz, L. Romera, Crashworthiness study on hybrid energy absorbers as vertical struts in civil aircraft fuselage designs, International Journal of Crashworthiness 0 (2019) 1–17. doi:10.1080/13588265.2019.1605723.

[3] J. Paz, J. Díaz, L. Romera, F. Teixeira-Dias, Optimisation of thin-walled hybrid vertical struts for crashworthy aircraft designs, Structural and Multidisciplinary Optimization 61 (2020) 141–158. doi:10.1007/s00158-019-02350-3.

[4] Y. Shi, P. Zhu, L. Shen, Z. Lin, Lightweight design of automotive front side rails with twb concept, Thin-walled structures 45 (2007) 8–14.

[5] F. Tarlochan, F. Samer, A. Hamouda, S. Ramesh, K. Khalid, Design of thin wall structures for energy absorption applications: enhancement of crashworthiness due to axial and oblique impact forces, Thin-Walled Structures 71 (2013) 7–17.

[6] J. Marsolek, H.-G. Reimerdes, Energy absorption of metallic cylindrical shells with induced non-axisymmetric folding patterns, International Journal of Impact Engineering 30 (2004) 1209–1223.

[7] Z. Ahmad, D. P. Thambiratnam, Application of foam-filled conical tubes in enhancing the crashworthiness performance of vehicle protective structures, International journal of crashworthiness 14 (2009) 349–363.

[8] W. J. Stronge, Impact mechanics, Cambridge university press, 2004.

[9] A. Alghamdi, Collapsible impact energy absorbers: an overview, Thin-walled structures 39 (2001) 189–213.

[10] W. Johnson, Metallic energy dissipating systems, Appl. Mech. Rev. 31 (1978) 277–288.

[11] G. Lu, T. Yu, Energy absorption of structures and materials, Elsevier, 2003.

[12] J. M. Alexander, An approximate analysis of the collapse of thin cylindrical shells under axial loading, Quarterly Journal of Mechanics and Applied Mathematics 13 (1960) 10–15.

[13] T. Wierzbicki, W. Abramowicz, On the crushing mechanics of thin-walled structures, Journal of Applied mechanics 50 (1983) 727–734.

[14] W. Abramowicz, T. Wierzbicki, Axial crushing of multicorner sheet metal columns, Journal of Applied Mechanics 56 (1989) 113–120.

[15] D. Hull, A unified approach to progressive crushing of fibre-reinforced composite tubes, Composites science and technology 40 (1991) 377–421.

[16] W. Abramowicz, N. Jones, Dynamic progressive buckling of circular and square tubes, International Journal of Impact Engineering 4 (1986) 243–270.

[17] S. Guillow, G. Lu, R. Grzebieta, Quasi-static axial compression of thin-walled circular aluminium tubes, International Journal of Mechanical Sciences 43 (2001) 2103–2123.

[18] S. Salehghaffari, M. Tajdari, M. Panahi, F. Mokhtarnezhad, Attempts to improve energy absorption characteristics of circular metal tubes subjected to axial loading, Thin-Walled Structures 48 (2010) 379–390.

[19] M. Sadeghi, Design of heavy duty energy absorbers, Structural Impact and Crashworthiness, 2 (1984) 588–604.

[20] S. Reid, Metal tubes as impact energy absorbers, Metal forming and impact mechanics (1985) 249.

[21] K. Andrews, G. England, E. Ghani, Classification of the axial collapse of cylindrical tubes under quasi-static loading, International Journal of Mechanical Sciences 25 (1983) 687–696.

[22] N. Jones, Structural impact, Cambridge university press, 2011.

[23] A. K. Noor, H. D. Carden, Computational methods for crashworthiness (1993).

[24] P. Zhu, F. Pan, W. Chen, F. A. Viana, Lightweight design of vehicle parameters under crashworthiness using conservative surrogates, Computers in Industry 64 (2013) 280–289.

[25] S. Jeong, S. Yoon, S. Xu, G. Park, Non-linear dynamic response structural optimization of an automobile frontal structure using equivalent static loads, Proceedings of the Institution of Mechanical Engineers, Part D: Journal of Automobile Engineering 224 (2010) 489–501.

[26] J. Will, H. Baldauf, C. Bucher, Robustness evaluations in virtual dimensioning of passive passenger safety and crashworthiness, Proceedings Weimarer Optimierungs-und Stochastiktage (2006) 24.

[27] F. Duddeck, Multidisciplinary optimization of car bodies, Structural and Multidisciplinary Optimization 35 (2008) 375–389. doi:10.1007/s00158-007-0130-6.

[28] X. Song, G. Sun, Q. Li, Sensitivity analysis and reliability based design optimization for high-strength steel tailor welded thin-walled structures under crashworthiness, Thin-Walled Structures 109 (2016) 132–142. URL: https://linkinghub.elsevier.com/retrieve/pii/S0263823116305924. doi:10.1016/j.tws.2016.09.003.

[29] B. Gao, Y. Ren, H. Jiang, J. Xiang, Sensitivity analysis-based variable screening and reliability optimisation for composite fuselage frame crash-

worthiness design, International Journal of Crashworthiness 24 (2019) 380–388. doi:10.1080/13588265.2018.1454289.

[30] J. Fang, G. Sun, N. Qiu, N. H. Kim, Q. Li, On design optimization for structural crashworthiness and its state of the art, Structural and Multidisciplinary Optimization 55 (2017) 1091–1119.

[31] Y. Ren, J. Xiang, Crashworthiness uncertainty analysis of typical civil aircraft based on box–behnken method, Chinese Journal of Aeronautics 27 (2014) 550–557. doi:10.1016/j.cja.2014.04.020.

[32] M. Rais-Rohani, K. N. Solanki, E. Acar, C. D. Eamon, Shape and sizing optimisation of automotive structures with deterministic and probabilistic design constraints, International journal of vehicle design 54 (2010) 309–338.

[33] Y. Fu, K. H. Sahin, Better optimization of nonlinear uncertain systems (bonus) for vehicle structural design, Annals of Operations Research 132 (2004) 69–84.

[34] D. Lönn, Ø. Fyllingen, L. Nilssona, An approach to robust optimization of impact problems using random samples and meta-modelling, International Journal of Impact Engineering 37 (2010) 723–734.

[35] L. Farkas, D. Moens, S. Donders, D. Vandepitte, Optimisation study of a vehicle bumper subsystem with fuzzy parameters, Mechanical systems and signal processing 32 (2012) 59–68.

[36] G. Eichmueller, M. Meywerk, On computer simulation of components for automotive crashworthiness: validation and uncertainty quantification for simple load cases, International Journal of Crashworthiness (2019) 1–13. doi:10.1080/13588265.2019.1582577.

[37] G. Sun, G. Li, S. Zhou, H. Li, S. Hou, Q. Li, Crashworthiness design of vehicle by using multiobjective robust optimization, Structural and Multidisciplinary Optimization 44 (2011) 99–110.

[38] Y. Zhang, P. Zhu, G. Chen, Lightweight design of automotive front side rail based on robust optimisation, Thin-walled structures 45 (2007) 670–676.

[39] M. Moustapha, B. Sudret, J.-M. Bourinet, B. Guillaume, Adaptive kriging reliability-based design optimization of an automotive body structure under crashworthiness constraints, in: Proceedings of the 12th International Conference on Applications of Statistics and Probability in Civil Engineering (ICASP12), Vancouver, Canada, July 12-15, University of British Columbia, 2015.

[40] S. Zhang, P. Zhu, W. Chen, P. Arendt, Concurrent treatment of parametric uncertainty and metamodeling uncertainty in robust design, Structural and Multidisciplinary Optimization 47 (2013) 63–76. doi:10.1007/s00158-012-0805-5.

[41] N. Qiu, Y. Gao, J. Fang, G. Sun, Q. Li, N. H. Kim, Crashworthiness optimization with uncertainty from surrogate model and numerical error, Thin-Walled Structures 129 (2018) 457–472. doi:10.1016/j.tws.2018.05.002.

[42] S. Zhang, P. Zhu, W. Chen, Crashworthiness-based lightweight design problem via new robust design method considering two sources of uncertainties, Proceedings of the Institution of Mechanical Engineers, Part C: Journal of Mechanical Engineering Science 227 (2013) 1381–1391.

[43] C. Gilkeson, V. Toropov, H. Thompson, M. Wilson, N. Foxley, P. Gaskell, Dealing with numerical noise in CFD-based design optimization, Computers & Fluids 94 (2014) 84–97. doi:10.1016/j.compfluid.2014.02.004.

[44] W. Abramowicz, N. Jones, Dynamic progressive buckling of circular and square tubes, International Journal of Impact Engineering 4 (1986) 243–270.

[45] F. J. Plantema, Collapsing stresses of circular cylinders and round tubes, Report S. 280, Nat Luchtvaartlaboratorium, The Netherlands (1964).

[46] G. Hendeby, F. Gustafsson, On nonlinear transformations of gaussian distributions, Technical Report from Automatic Control at Link pings Universitet (2007).

[47] A. Pugsley, The crumpling of tubular structures under impact conditions, in: Proc. of the Symposium on the use of aluminium in railway rolling stock. Institute of Locomotive Engineers. The Aluminium Development Association, 1960, pp. 22–41.

[48] P. Thornton, H. Mahmood, C. Magee, Energy absorption by structural collapse, in: N. Jones, T. Wierzbicki (Eds.), Structural crashworthiness, Butterworths, London, 1983, pp. 96–117.

[49] W. Abramowicz, N. Jones, Dynamic axial crushing of square tubes, International Journal of Impact Engineering 2 (1984) 179–208.

[50] W. Abramowicz, The effective crushing distance in axially compressed thin-walled metal columns, International Journal of Impact Engineering 1 (1983). doi:10.1016/0734-743x(83)90025-8.

[51] S. P. Timoshenko, J. M. Gere, Theory of elastic stability, Courier Corporation, 2009.

[52] M. McKay, R. Beckman, W. Conover, A comparison of three methods for selecting values of input variables in the analysis of output from a computer code, Technometrics 21 (1979) 239–245.

[53] L. P. Swiler, G. D. Wyss, A User's Guide to Sandia's Latin Hypercube Sampling Software: LHS UNIX Library Standalone Version. SAND2004-2439, Technical Report, Sandia National Laboratories, Albuquerque, NM, USA, 2004.

[54] K. R. Salbey, A. A. Giunta, M. D. Richards, E. C. Cyr, L. P. Swiler, S. L. Brown, M. S. Eldred, B. Adams, Surfpack User's Manual Version 1.1, Technical Report, Sandia National Laboratories, Albuquerque, NM, USA, 2013.

[55] D. G. Krige, A statistical approach to some basic mine valuation problems on the witwatersrand, Journal of the Chemical, Metallurgical and Mining Engineering Society of South Africa (1951) 119–139.

[56] G. Matheron, Principles of geostatistics, Economic geology 58 (1963) 1246–1266.

[57] J. Friedman, C. Roosen, An introduction to multivariate adaptive regression splines., Statistical methods in medical research 4 (1995) 197–217.

[58] J. Neter, M. H. Kutner, C. J. Nachtsheim, W. Wasserman, Applied linear statistical models, volume 4, Irwin Chicago, 1996.

[59] A. Nealen, A short-as-possible introduction to the least squares, weighted least squares, and moving least squares methods for scattered data approximation and interpolation., Technical report, Discrete Geometric Modeling Group, Technishe Universität, Berlin, Germany (2004).

[60] P. Lancaster, K. Salkauskas, Surfaces generated by moving least squares methods, Mathematics of Computation 37 (1981) 141–158.

[61] ABAQUS 2017 Documentation, Dassault Systèmes, 2017.

[62] SAE Standard J211: Instrumentation for Impact Test, Technical Report, Safety Test Instrumentation Stds Comm, 1995.

[63] M. Huang, Vehicle Crash Mechanics, CRC Press, 2002.

[64] Q. Zhou, P. Jiang, X. Huang, F. Zhang, T. Zhou, A multi-objective robust optimization approach based on gaussian process model, Structural and Multidisciplinary Optimization 57 (2018) 213–233.

[65] J. Qian, J. Yi, J. Cheng, J. Liu, Q. Zhou, A sequential constraints updating approach for kriging surrogate model-assisted engineering optimization design problem, Engineering with Computers (2019) 1–17.

[66] S. Hsu, N. Jones, Quasi-static and dynamic axial crushing of thin-walled circular stainless steel, mild steel and aluminium alloy tubes, International Journal of Crashworthiness 9 (2004) 195–217.

[67] N. Jones, Energy absorption effectiveness of thin-walled structures under static and dynamic axial crushing loads, Impact loading of lightweight structures, edited by M. Alves & N. Jones. WIT Press, Boston, US, and Southampton, UK (2005) 273–87.

Appendix A. Analytical propagation of uncertainty

The analytical uncertainty propagation of the formulas presented in section 2 is now described. Considering the formula from equation (1) as means of example (an homologous procedure is also used with equations (9) and (10)), it is first divided into a coefficient and two simpler functions as

$$P_{\text{c-mean}}^{\text{emp}} = 72.3(D/t_{\text{c}})^{0.32}\sigma_0\, t_{\text{c}}^2/4 = \alpha_1 g(D)\, h(t_{\text{c}}), \tag{A.1}$$

where

$$\alpha_1 = 72.3\sigma_0/4, \tag{A.2}$$

$$g(D) = D^{0.32}, \quad \text{and} \tag{A.3}$$

$$h(t_{\text{c}}) = t_{\text{c}}^{1.68}. \tag{A.4}$$

With the formula divided, now the expected value $E[\ ]$ and variance $V[\ ]$ can be calculated using the following properties of the statistical moments:

$$E[\alpha_1 g(D)\, h(t_{\text{c}})] = \alpha_1 E[g(D)]\, E[h(t_{\text{c}})], \tag{A.5}$$

$$V[\alpha_1 g(D)\, h(t_{\text{c}})] = \alpha_1^2 (E^2[g(D)]\, V[h(t_{\text{c}})] + V[g(D)]\, E^2[h(t_{\text{c}})] + V[g(D)]\, V[h(t_{\text{c}})]), \tag{A.6}$$

where

$$E[g(D)] = g(D)|_{E[D]}, \tag{A.7}$$

$$E[h(t_{\text{c}})] = h(t_{\text{c}})|_{E[t_{\text{c}}]}. \tag{A.8}$$

Moreover, to calculate the variance of $g(D)$ and $h(t_{\text{c}})$, the following approximations using second-order Taylor expansion series are used

$$V[g(D)] = \left(\left.\frac{dg(D)}{dD}\right|_{E[D]} \right)^2 V[D] + \frac{1}{2}\left(\left.\frac{d^2 g(D)}{dD^2}\right|_{E[D]} \right)^2 V^2[D] + R(D), \tag{A.9}$$

$$V[h(t_{\text{c}})] = \left(\left.\frac{dh(t_{\text{c}})}{dt_{\text{c}}}\right|_{E[t_{\text{c}}]} \right)^2 V[t_{\text{c}}] + \frac{1}{2}\left(\left.\frac{d^2 h(t_{\text{c}})}{dt_{\text{c}}^2}\right|_{E[t_{\text{c}}]} \right)^2 V^2[t_{\text{c}}] + R(t_{\text{c}}), \tag{A.10}$$

where R is the higher order error in each Taylor series. After coupling the formulas with equations (A.5) and (A.6), it results in

$$E[P_{\text{c-mean}}^{\text{emp}}] = E[\alpha_1\, g(D)\, h(t_{\text{c}})] = \alpha_1\, g(D)|_{E[D]}\, h(t_{\text{c}})|_{E[t_{\text{c}}]}, \tag{A.11}$$

$$V[P_{\text{c-mean}}^{\text{emp}}] = V[\alpha_1\, g(D)\, h(t_{\text{c}})] \approx \alpha_1^2 \left\{ \left(g(D)|_{E[D]} \right)^2 \left[\left(\left.\frac{dh(t_{\text{c}})}{dt_{\text{c}}}\right|_{E[t_{\text{c}}]} \right)^2 V[t_{\text{c}}] + \frac{1}{2}\left(\left.\frac{d^2 h(t_{\text{c}})}{dt_{\text{c}}^2}\right|_{E[t_{\text{c}}]} \right)^2 V^2[t_{\text{c}}] \right] + \right.$$

$$+ \left(h(t_{\text{c}})|_{E[t_{\text{c}}]} \right)^2 \left[\left(\left.\frac{dg(D)}{dD}\right|_{E[D]} \right)^2 V[D] + \frac{1}{2}\left(\left.\frac{d^2 g(D)}{dD^2}\right|_{E[D]} \right)^2 V^2[D] \right] +$$

$$+ \left. \left[\left(\left.\frac{dh(t_{\text{c}})}{dt_{\text{c}}}\right|_{E[t_{\text{c}}]} \right)^2 V[t_{\text{c}}] + \frac{1}{2}\left(\left.\frac{d^2 h(t_{\text{c}})}{dt_{\text{c}}^2}\right|_{E[t_{\text{c}}]} \right)^2 V^2[t_{\text{c}}] \right] \left[\left(\left.\frac{dg(D)}{dD}\right|_{E[D]} \right)^2 V[D] + \frac{1}{2}\left(\left.\frac{d^2 g(D)}{dD^2}\right|_{E[D]} \right)^2 V^2[D] \right] \right\}. \tag{A.12}$$

As a last step, if equations (A.11) and (A.12) are particularized for $D \sim \mathcal{N}(\mu_{\text{D}}, \sigma_{\text{D}}^2)$ and $t_{\text{c}} \sim \mathcal{N}(\mu_{\text{t}_{\text{c}}}, \sigma_{\text{t}_{\text{c}}}^2)$, the following expressions are obtained:

$$E[P_{\text{c-mean}}^{\text{emp}}] = \alpha_1\, g(\mu_{\text{D}})\, h(\mu_{\text{t}_{\text{c}}}), \tag{A.13}$$

$$V[P_{\text{c-mean}}^{\text{emp}}] \approx \alpha_1^2 \left[g(\mu_{\text{D}})^2 \left(h'(\mu_{\text{t}_{\text{c}}})^2 \sigma_{\text{t}_{\text{c}}}^2 + \frac{1}{2} h''(\mu_{\text{t}_{\text{c}}})^2 \sigma_{\text{t}_{\text{c}}}^4 \right) + h(\mu_{\text{t}_{\text{c}}})^2 \left(g'(\mu_{\text{D}})^2 \sigma_{\text{D}}^2 + \frac{1}{2} g''(\mu_{\text{D}})^2 \sigma_{\text{D}}^4 \right) + \right.$$

$$+ \left. \left(h'(\mu_{\text{t}_{\text{c}}})^2 \sigma_{\text{t}_{\text{c}}}^2 + \frac{1}{2} h''(\mu_{\text{t}_{\text{c}}})^2 \sigma_{\text{t}_{\text{c}}}^4 \right) \left(g'(\mu_{\text{D}})^2 \sigma_{\text{D}}^2 + \frac{1}{2} g''(\mu_{\text{D}})^2 \sigma_{\text{D}}^4 \right) \right]. \tag{A.14}$$